

DEVELOPMENTAL BIOLOGY

Acute multidrug delivery via a wearable bioreactor facilitates long-term limb regeneration and functional recovery in adult *Xenopus laevis*

Nirosha J. Murugan^{1,2}, Hannah J. Vigran^{1,2}, Kelsie A. Miller^{1,2}, Annie Golding^{2,3}, Quang L. Pham^{2,3}, Megan M. Sperry^{1,4}, Cody Rasmussen-Ivey^{1,2}, Anna W. Kane^{1,2,4}, David L. Kaplan^{2,3}, Michael Levin^{1,2,4*}

Limb regeneration is a frontier in biomedical science. Identifying triggers of innate morphogenetic responses in vivo to induce the growth of healthy patterned tissue would address the needs of millions of patients, from diabetics to victims of trauma. Organisms such as *Xenopus laevis*—whose limited regenerative capacities in adulthood mirror those of humans—are important models with which to test interventions that can restore form and function. Here, we demonstrate long-term (18 months) regrowth, marked tissue repatterning, and functional restoration of an amputated *X. laevis* hindlimb following a 24-hour exposure to a multidrug, pro-regenerative treatment delivered by a wearable bioreactor. Regenerated tissues composed of skin, bone, vasculature, and nerves significantly exceeded the complexity and sensorimotor capacities of untreated and control animals' hypomorphic spikes. RNA sequencing of early tissue buds revealed activation of developmental pathways such as Wnt/ β -catenin, TGF- β , hedgehog, and Notch. These data demonstrate the successful “kickstarting” of endogenous regenerative pathways in a vertebrate model.

INTRODUCTION

The longstanding goal of regenerating whole complex organs has remained elusive despite receiving considerable attention from developmental and regenerative biology. The prevalence of human limb loss in the United States alone is expected to increase substantially over the next 30 years, affecting 3.6 million individuals per year by 2050 (1), leaving diabetics, veterans of war, trauma survivors, and those suffering from peripheral artery disease with limited options in the event of an amputation. Despite significant technological advances, clinicians still lack tools to facilitate the recovery or reversal of tissue loss, while prosthetics offer only limited functional restoration of the patient's own limbs. Moreover, unlike single-purpose mechanoelectrical appendages, developing regenerative methodologies targeting limbs might be instructive in the regeneration of other organs. Thus, identifying and potentiating the underlying programs that drive limb regrowth would be of great interest to medical and research fields.

Previous efforts attempted to induce limb regeneration in nonregenerative models with the use of electrical stimulation (2–6), tissue-guiding biomaterials (7), progenitor cell transplantation (8–10), and the direct up-regulation of key molecular pathways (11, 12). However, all reports of experimentally stimulating regeneration have largely involved fully or partially regenerative model systems such as axolotls, anurans on the boundary of regeneration, or developmentally immature (i.e., nonadult) phenotypes (13–16). Limited success has been reported in restoring substantial growth and patterning of new functional limbs in nonregenerative adults. While previous approaches have focused on driving specific facets of the process, limb restoration requires the spatial and temporal coordination of cell

types, signaling cascades, and structural support to generate the necessary cues that organize cells into heterogeneous, intricately patterned, three-dimensional (3D) structures. Thus, an important new direction for the field of regenerative medicine is the discovery of interventions that trigger latent developmental or embryonic cascades (17, 18), shifting the burden of morphogenetic control onto the cells and tissues themselves. Combinations of electrochemical and biomaterial-based treatments would further overcome previous pitfalls by offering both information-rich signals and structural stability. Furthermore, the development of a biomimetic technology, which interfaces with the wound site, represents an advantageous strategy, as creating a highly controlled microenvironment during the early key stages of tissue repair can provide the necessary instruction and guidance to reestablish structural-functional normalcy.

To generate an effective multimodal treatment, development of tractable vertebrate models with human-like limitations of limb regeneration abilities is essential (19). One such model is the anuran amphibian, *Xenopus laevis*—a common system that has previously been used to address questions in developmental biology and regenerative medicine (20). Like mammals, adult *X. laevis* exhibits modest tissue renewal, few pluripotent stem cell pools, and an age-dependent decline of regenerative ability that is similar to that of human finger amputations (21, 22).

While *X. laevis* are capable of fully regenerating most of their tissues including their hindlimbs before metamorphosis in tadpole stages, their ability to marshal a regenerative response greatly declines with maturation (23, 24). The temporal restriction of regenerative competence makes *Xenopus* an ideal model system for determining characteristics that enable or inhibit regeneration. Molecular evidence using small-molecule inhibitors delivered via single-drug delivery methods has validated that BMP (bone morphogenetic protein) (25), FGF (fibroblast growth factor) and Wnt (26, 27), Shh (28), and Nodal/transforming growth factor- β (TGF- β) (29, 30) signaling pathways are required for proper formation of the regenerated tail in tadpoles, paralleling their involvement in early embryonic patterning.

¹Department of Biology, Tufts University, Medford, MA, USA. ²Allen Discovery Center at Tufts University, Medford, MA, USA. ³Department of Biomedical Engineering, Tufts University, Medford, MA, USA. ⁴Wyss Institute for Biologically Inspired Engineering, Harvard University, Boston, MA, USA.

*Corresponding author. Email: michael.levin@tufts.edu

Classically regenerative organisms overcome limitations of growth and tissue repatterning by forming a blastema: a temporary construct, derived from nonepithelial tissues, of progenitors that gradually re-establishes the lost body part (14). While premetamorphic *Xenopus* are regeneratively competent in this way, their abilities diminish with age as stocks of progenitors are lost during the pre- to post-metamorphic transition, rendering them unable to regrow limbs when an injury is incurred during adulthood.

Despite these advancements toward understanding the complexity of limb regeneration, most studies have relied on anurans in developmental stages when they still retain regenerative competency, such as full-regenerative tadpoles, or post-metamorphic or froglets before full transformation to adult frogs, which are animals at the boundary of regenerative competency (31). Unlike tadpoles or froglets, adult *Xenopus* fail to regenerate their hindlimbs upon experimental amputation, instead generating featureless cartilaginous spikes (32). Our recent work in adult *Xenopus* showed a significant degree of outgrowth induced by progesterone (33). However, the resulting regenerate was far from fully functional and repatterned limbs were not achieved. Thus, a more sophisticated distal patterning of the limb and the achievement of function and sensorimotor integration represent a key goal of current research.

Here, we developed a complex intervention for adult *Xenopus* hind-leg amputations to address several key open aspects of the limb regeneration roadmap. First, we used a wearable bioreactor (“BioDome”) (34, 35) to attain control over the local microenvironment of a wound in vivo. In addition, we sought to use compounds that could trigger a sustainable, endogenous morphogenetic cascade without subsequent intervention or continuous micromanagement by choosing a variety of compounds that would induce complementary processes such as the modulation of inflammation, promotion of neural sparing, and tissue growth.

We demonstrated that following hindlimb amputation in adult *Xenopus*, a very brief (just 24-hour) exposure to a wearable bioreactor containing silk protein infused with five small-molecule compounds induced marked tissue outgrowth, patterning, and gain of sensorimotor function. Treated animals displayed a marked delay of wound closure, followed by long-term (18-month) growth outcomes including increased bone length, soft tissue patterning, and neuromuscular repair. Histologically, the regenerating limbs contained nerves, smooth muscle displaying integration of blood vessels, and reorganization of the extracellular matrix (ECM) proteins involved in tissue remodeling. Transcriptomic analysis identified immediate and short-term molecular effects of amputation and our subsequent intervention in terms of signal pathway inductions and transcriptional effects. These early events were translated to long-term anatomical repatterning. Regenerated bone displayed anatomical feature characteristic of wild-type morphology, and distal limb soft tissue displayed digit-like projections. Most notably, the animals used the newly formed limb to ambulate in a manner similar to that of wild-type frogs. Last, we determined that sensorimotor pathways were functionally restored to preinjury levels in the animals exposed to the full treatment condition, indicating reestablishment of afferent sensory nerve fibers and neuromuscular tissue interfaces.

Our data demonstrated that the nonregenerative adult *Xenopus* system can be induced toward a sustained regenerative state by a brief targeted chemical trigger. That is to say, endogenous but latent regenerative competency was restored to regrow and remodel a missing limb. The induction method did not require gene therapy

or stem cell implants but produced molecular, cellular, and tissue-level changes that restored limb morphology and sensorimotor function. This provides a proof of principle for kickstarting complex organ regeneration responses in vertebrate models using compound interventions consisting of a drug blend and a wearable bioreactor delivery device.

MATERIALS AND METHODS

Animals

Adult female *X. laevis* ($n = 115$) measuring 5 to 6.25 cm (nose to tail) were purchased from a licensed vendor (Nasco, Fort Atkinson, WI) and allowed to acclimate to holding tanks for 2 weeks before experimentation. Animals were maintained at 18°C in 10-liter plastic tanks containing a defined frog water (Reef Salt, Seachem Laboratories, ~1.65-kilohm conductivity, 7.8 to 8.0 pH) and exposed to 12-hour light-dark cycles. Before surgery, animals were soaked in a broad-spectrum gentamicin antibiotic for 2 hours (Gibco, Fisher Scientific, USA) to minimize bacterial contamination of the limb stump after amputation. Handling and experimentation procedures were approved by Tufts University’s Institutional Animal Care and Use Committees.

Limb amputation

Hindlimb amputation surgeries were carried out according to previously established protocols (33, 34). Briefly, animals were first anesthetized by full-body immersion in buffered frog water containing 0.05% benzocaine. Upon loss of toe pinch reflex, buprenorphine (75 mg/kg) was injected subcutaneously just below the lateral line on the contralateral side to the leg that would be amputated. Right hindlimbs were amputated at the midpoint of the tibiofibular bone with a sterile microsurgical blade using a straight cut. No bone resection was performed, nor was a tissue flap sewn over the wound site. Following hemostasis, animals regained consciousness and were allowed to recover in sterile frog water for a minimum of 60 min.

Device attachment

Animals were randomly assigned to one of three treatment conditions: No device, BioDome only, or BioDome with cocktail treatment (described in “BioDome fabrication” and “Cocktail composition” sections). The device attachment procedure was preceded by a second anesthetization [0.05% benzocaine soak and buprenorphine (75 mg/kg)]. Unconscious animals were then fitted with devices that were affixed to the amputation site stump using monofilament surgical sutures (7-0 Monosof, 18” P-16 cutting, Covidien, USA). Two sutures were placed through the dermal layer on either side of the leg. These stitches were sufficient to hold the device in place and did not damage the underlying deep fascial layers. Following attachment, animals were returned to their home tanks, whereupon they regained consciousness and were allowed to swim freely. Control animals were handled similarly to those that received devices, but no devices were attached to the wound stump.

Device removal and maintenance

After 24 hours, animals were anesthetized and treated with an analgesic as previously described. The devices were then removed by cutting the single suture on either side of the leg, and the frogs were placed back into tanks containing a fungicide (Kordon methylene blue at concentrations of 1 ml/10 liter frog water). After another

24 hours, the water was replaced with fresh 100% frog water. Once their devices were removed, animals were maintained for 18 months in frog water that was changed daily. Endpoint euthanasia was carried out by full-body immersion in frog water with 0.2% benzocaine. Regenerates and contralateral limbs were collected and processed for histological analysis (see the “Histology and immunohistochemistry” section).

BioDome fabrication

The BioDomes were composed of a soft silicon insert that contained silk hydrogels as a controlled-release substrate and drug carrier. The fabrication of the device has been reported elsewhere (34). Briefly, the outer cylindrical silicon sleeve (20-mm H × 18-mm D) was fabricated by casting silicon elastomer (Dragon skin 10, Smooth-on, Macungie, PA) against a 3D-printed mold, which was designed using CAD software (SolidWorks, Waltham, MA, USA) and printed using a Formlabs 3D printer (Somerville, MA, USA).

Silk processing

Silk solution was prepared following a previously published protocol (36). Briefly, 5 g of silkworm (*Bombyx mori*) cocoons (Tajima Shoji, Yokohama, Japan) was cut and degummed in a solution of 0.02 M sodium carbonate (Na₂CO₃) for 45 min to remove nonessential protein substrates (i.e., sericin). Fibers were washed in deionized (DI) water several times to remove the Na₂CO₃ and then dried inside a fume hood overnight at 22°C. Dry silk fibers were then dissolved in a 20% (w/v) solution of 9.3 M lithium bromide (Sigma-Aldrich, St. Louis, MO) and placed in an oven set to 60°C for 4 hours. The solution was then dialyzed in DI water using a dialysis cassette [molecular weight cutoff (MWCO) of 3.5 kDa, Thermo Fisher Scientific, Waltham, MA] with gentle stirring. Water was changed six times over a 48-hour period. The dialyzed solution was centrifuged three times at 13,000g, 4°C for 20 min each followed by filtering through a cell strainer (40-μm pore size, Thermo Fisher Scientific) to remove impurities. To determine the concentration of the filtered solution, a 0.5-ml sample was dried completely overnight in an oven. Having evaporated the water content, the dried silk was weighed and the concentration in % (w/v) was calculated as the ratio of the weight of the dried silk over its initial volume of 0.5 ml. The hydrogels were prepared with a final concentration of 3% (w/v) silk solution, horseradish peroxidase of 20 U/ml, and hydrogen peroxide (H₂O₂) of 0.01% (w/v). The liquid solution was poured into the silicon sleeve and allowed to gel for 30 min before attachment to the limb stump of the animal (37). Gel compression strength and moduli of the gels were tested as previously published (34).

Cocktail composition

For the cocktail-loaded devices, 1,4-dihydrophenanthrolin-4-one-3-carboxylic acid (1,4-DPCA) (0.014 μg/ml) (catalog no. 71220, Cayman Chemicals, MI, USA), brain-derived neurotrophic factor (BDNF) (0.5 μg/ml) (catalog no. 450-02, PeproTech, MA, USA), growth hormone (GH) (0.5 μg/ml) (catalog no. 100-40, PeproTech, MA, USA), resolvin D5 (RD5) (0.036 μg/ml) (catalog no. 10007280, Cayman Chemicals, MI, USA), and retinoic acid (RA) (0.015 μg/ml) (catalog no. 11017, Cayman Chemicals, MI, USA) were loaded into the liquid silk solution before insertion and gelation into the silicon sleeve. All concentrations were determined on the basis of effects in the literature discussed previously and scaled to the weight and age of the animals.

In vitro release studies

To determine the release profiles of the drugs used in the study, 50 μl of each hydrogel solution loaded with specific amounts of the drugs was added into 1.5-ml microcentrifuge tubes and incubated for 45 min at 37°C to a complete gelation. Then, 1 ml of Dulbecco's phosphate-buffered saline (1×, Gibco) was added into each vial followed by incubation at 37°C. At fixed time points, 300 μl of supernatant was collected for analysis. Release solutions of drug-free silk hydrogels were used as controls. Standard curves were determined by measuring the optical density of solutions with known concentrations. All the release experiments were carried out in triplicate. For RA and 1,4-DPCA, optical density of the release solutions was determined on an ultraviolet-transparent 96-well plate (Corning, Corning, NY) using a SpectraMax M2 microplate reader (Molecular Devices, San Jose, CA) operated by SoftMax Pro 6 software. Detection was performed at a wavelength of 280 and 350 nm for 1,4-DPCA and RA solutions, respectively. The concentrations of BDNF and GH in the release samples were determined using enzyme-linked immunosorbent assay (ELISA) kits containing monoclonal antibodies designed for BDNF and GH (#BGK23560 and #BGK01241, PeproTech, Rocky Hill, NJ, USA). Sample preparation and measurement were performed according to the manufacturer's protocol. Optical density of the samples was read at 450 nm using a SpectraMax M2 plate reader. Release samples of RD5 were filtered with a protein filtration column (MWCO = 3 kDa; Thermo Fisher Scientific, #UFC500324) to remove the high-molecular weight fibroin content. Then, optical density of the samples was determined at a wavelength of 244 nm using a SpectraMax M2 plate reader.

Soft tissue imaging

At regular intervals over the 18-month maintenance period, animals were evaluated for soft tissue repatterning and bone regrowth. Animals were anesthetized as described previously, and high-resolution images of their wound sites were captured using a digital single-lens reflex (DSLR) camera (Canon EOS Rebel T7i) with a ruler in frame for calibrated measurements. To ensure replicability, the amputation plane served as a standard reference point for all measurements. The site of amputation was easily identified due a reliable tapering of the limb at the point of incision. Each measurement consisted of a linear assessment of length between the amputation site and the most distal end of the regenerate.

In vivo x-ray and micro-CT imaging of bone

In addition to soft tissue measurements, bone length was assessed using a handheld x-ray device (Nomad Pro 2TM) using standard imaging settings of 60 kV, 2.5 mA for 0.20-s exposure time. This imaging protocol was consistent with previous work (33, 34). Every animal was subjected to the same dose (0.12 mSv) at fixed time points. Computerized tomography (CT) in a vivaCT 40 scanner was performed to visualize the detailed microarchitecture of bone at the end of the 18-month regeneration period following euthanasia by benzocaine overdose (0.2% full-body immersion). Distal trabecular bone and midshaft cortical bone sections (615 slices per animal, 76 μm per slice, integration time of 300 ms) were visualized and rendered into 3D images for further quantification. The radiation dose was established by manufacturer guidelines using local CT dose index, which ranged from 453 to 1255 mGy.

Histology and immunohistochemistry

Histological analyses were carried out on regenerates and contralateral limbs at fixed intervals over time. Tissues were collected at 18 months

post-amputation (mpa). Long-term regenerate tissues were fixed overnight in 4% paraformaldehyde (PFA) in phosphate-buffered saline (PBS) and decalcified for 2 weeks by exposure to increasing concentrations (10 to 15%) of EDTA (pH7.4). Once decalcified (confirmed using x-ray), tissues were gradually equilibrated to 30% sucrose before embedding in optimum cutting temperature (OCT) (Sakura Finetek, USA). Samples were frozen in liquid nitrogen. Limb tissues were serially sectioned at 14 μ m using a cryostat (Leica CM1850) and placed on glass slides. Cross sections were taken at 14- μ m intervals across the limb from the tibiofibular region above the original amputation site to the patterned region at the terminus of the limb. To visualize the patterning, the end portion of the limb was sectioned horizontally at 14- μ m intervals. Sections were dried for at least an hour before storage at -80°C .

For immunohistochemistry, slides were equilibrated to room temperature for at least 2 hours before staining. Slides were post-fixed for 5 min in 4% PFA and then blocked in blocking buffer (PBS with 0.1% Triton X-100 and 10% normal goat serum) for 1 hour. Primary antibodies against acetylated α -tubulin (AAT) (1:100), smooth muscle actin (SMA) (1:100), laminin (1:100) (Sigma-Aldrich, USA), TGF- β (1:250), fibronectin (1:500), and phosphohistone H3 (1:250) (Cell Signaling Technology, USA) were used. Slides were stained individually with each antibody except anti-SMA and anti-laminin, which were stained together. Primary antibodies were incubated on the slides overnight. After washing in PBS, Alexa Fluor secondaries (1:500; Thermo Fisher Scientific) were applied in blocking buffer for 2 hours. Slides were again washed in PBS and stained with 4',6-diamidino-2-phenylindole (DAPI) 1:200 in PBS for 20 min. Slides were mounted in Fluoromount-G (Thermo Fisher Scientific) and cured for at least 24 hours before imaging. Sections were imaged using an EVOS FL automated imaging system (Thermo Fisher Scientific). Entire sections were imaged and stitched together for analysis.

Quantification of immunostained tissue sections

Images of immunostained sections were imported to ImageJ software and converted to 8-bit binary images, and particle counting was used to quantify positive staining of cells. Data were then exported for further analyses. All statistical analyses were performed in IBM SPSS version 20 software. Assumptions of normality were tested before the use of parametric testing including analyses of variance (ANOVAs), *t* tests, and correlational analyses (Pearson's *r*). Nonparametric analyses, Mann-Whitney *U* test, Wilcoxon test, or Kruskal-Wallis test was conducted for comparison, where the data were not normally distributed. Significant differences were revealed by *P* values < 0.05 (two-tailed hypothesis testing).

Assessment of sensorimotor thresholds

To evaluate the sensorimotor capability of the regenerate, animals were assessed at 18 mpa. Each animal was placed into a glass tank filled with 2 liters of frog water and acclimated for 5 min until movement ceased completely. A video camera (iPod Touch 5th generation, Apple, CA, USA) was placed over the enclosure to capture recordings of the testing procedure. Standardized Von Frey (VF) filaments (Touch Test, Stoelting, IL, USA) were used to assess the sensory threshold of the regenerates. Filaments ranging from 0.008g to 300g in force were applied to the distal portion of the regenerate, from lowest to highest force. The first filament that induced a clear response (movement from the stationary position) was recorded. Animals were tested twice over a 2-day period, and the average threshold was reported.

Statistical analysis

All statistical analyses were performed using IBM SPSS v20. First, data were tested for homoscedasticity by Levene's test. Unifactorial analysis was performed on normally distributed data by unpaired, two-tailed Student's *t* test (two independent groups) or one-way ANOVA test (multiple independent groups) followed by post hoc Scheffe's test (when $P < 0.05$). When variable "time" was considered, a bifactorial analysis was performed by two-way ANOVA. Statistically significant differences between treatment groups (No device, Bio-Dome only, and cocktail treatment) at each specific time point were determined by using Student's *t* test. In nonnormal distributed data, a Kruskal-Wallis test followed by post hoc Dunn test (when $P < 0.05$) was conducted. The significance level was set to 0.05 in all cases. The statistical values are reported as means \pm SD or means \pm SEM, where indicated. When appropriate, dot or scatter plots are used for highlighting the individual variability within each experimental group.

RNA extraction

Following amputation, device attachment and removal, and 24 hours of treatment, regenerate tissues were harvested at 11, 24, and 72 hours post-amputation (hpa) for next-generation sequencing (NGS). Samples consisted of 1-cm-thick tissue blocks from the distal wound site. Tissue was extracted using TRIzol (Thermo Fisher Scientific) as per the manufacturer's protocol, and total RNA quality and quantity was assessed using a NanoDrop spectrophotometer (Thermo Fisher Scientific).

Next-generation sequencing

A total of 1.1 μ g of RNA was sent to the Tufts Genomic Core. RNA quality was assessed via bioanalyzer, and high-quality RNA was used for library preparation with the TruSeq Stranded RNA Library Prep Kit with RiboZero Gold (Invitrogen). Libraries were then multiplexed, and single-end, 50-nucleotide sequencing was performed on Illumina HiSeq 2500. Raw read files were sent to the Bioinformatics and Biostatistics Core at Joslin Diabetes Center.

NGS analysis

The reference genome for *X. laevis* was downloaded from the National Center for Biotechnology Information (NCBI) Genome database, assembly GCA_001663975.1. Reads were aligned using STAR aligner (38), and aligned reads were counted using featureCounts (39). Genes with expression counts more than 1 count per million (CPM) in at least three samples were included in the analysis, and counts were normalized by weighted trimmed mean of *M* values (40). Voom transformation was performed (41) to transform counts into logCPM, where $\text{CPM} = 1 \times 10^{+6} \times \text{count of a gene} / (\text{total counts of the sample} \times \text{normalization factor of the sample})$. Voom transformation also estimates the mean-variance relationship and uses it to compute appropriate observational-level weights so that more read depth gives more weights. To further down-weight the outliers, sample-specific quality weights (42) were collected and combined with the observational-level weights. Differentially expressed genes were identified using limma (43). Moderated *t* tests were performed to detect genes that were differentially expressed between two groups. Genes with false discovery rate (FDR) < 0.25 were considered significantly changed. Gene sets for pathway analysis were obtained from MSigDB Collections (www.gsea-msigdb.org/gsea/msigdb/collections.jsp), and gene sets that belong to canonical pathways or Gene Ontology (GO) were selected. Analysis

was performed with the Fry function in the rotation gene set test (Roast) in the limma R package (44). Gene sets that are coordinately up, coordinately down, and mixed all were considered significant if $P < 0.05$ and FDR < 0.05 .

Gene network analysis

Gene modules were identified by coexpression analysis in CEMiTool in R (Russo *et al.*, 2018) based on the logCPM values for control and cocktail-treated groups at 11 hours, 24 hours, and 7 days after limb amputation. In CEMiTool, a variance stabilizing transform was used to remove the dependence between mean and variance parameters. A percentage filter was applied to retain the mostly highly expressed genes for coexpression analysis (threshold of $P = 0.1$). Modules of coexpressing genes were identified within the dataset based on an automatically generated scaling value β ($\beta = 10$) and a minimum module size of 30 genes. To assess how the enrichment of these modules varied over time and group, module enrichment was calculated based on sample annotation. To determine which biological functions are associated with each module, overrepresentation analysis was performed using a pathway database from Reactome and pathways were considered to be significant for $P < 0.05$. Annotated module graphs combined gene-gene interaction data from Kyoto Encyclopedia of Genes and Genomes (KEGG) and Chemical and Genetic Perturbations to visualize the interacting genes contained in each module.

RESULTS

Twenty-four-hour exposure to a five-drug treatment induced bone regeneration and morphogenesis after hindlimb amputation

Adult *Xenopus* hindlimbs were amputated and fitted with silk hydrogel devices, known as the BioDome, which contained either the silk-hydrogel alone (BD) or the hydrogel loaded with the five pro-regenerative compounds (BDNF, 1,4-DPCA, RD5, GH, and RA), collectively known as MDT (multidrug treatment). Control animals were amputated and returned to their growth chambers without treatment (ND). After 24 hours, devices were removed, and animals were maintained without further intervention for up to 18 months with periodic assessment of regeneration of the hindlimb. The protracted observational window was selected based on Alibardi's (2018) model that predicted a 1.5-year latency to regenerate an anuran limb based on projections from serial measurements of newt stump diameters (Fig. 1A) (45).

Regenerative soft tissue length, as measured by the distance from the amputation plane to the distal tip of the regenerate, increased for all groups over the 18-month regeneration period, but animals exposed to MDT displayed significantly greater and complex soft tissue growth when compared to the other groups (Fig. 1B). This significant increase of soft tissue growth was observed as early as 2 weeks after amputation and was sustained throughout the growth period ($P < 0.05$; Fig. 1, B and C). BD and MDT hindlimbs grew comparably between months 6 and 8 ($P > 0.05$). However, beginning at 9 mpa, the MDT group displayed increased tissue length relative to all groups, which was sustained until the final measurements at 18 mpa ($P < 0.01$; Fig. 1, B and C). Thus, an exposure to MDT both increased regenerate length relative to all groups and initiated a secondary period of growth that was absent when no device was applied following amputation. These data demonstrate that a brief localized

application of the MDT to the amputation site can induce a greater and more sustained regenerative response.

In addition to regenerating longer hindlimbs, acute exposures to MDT changed the patterning complexity of the newly formed regenerate (Fig. 1C). Seventy-six percent of animals exposed to MDT displayed thicker, more complex regenerate morphologies relative to the featureless, heavily pigmented spikes of the ND group. Specifically, the distal segments of hindlimb regenerates associated with the MDT group presented as flattened, paddle-like structures with projecting pink or red hued tissue characteristic of digits at their distal ends (Fig. 1B). Animals exposed to the bioreactor without loaded chemical treatments (BD) generated intermediate phenotypes, with 20% of the animals displaying thicker cartilaginous spike-and-hook-like distal projections but with limited patterning (Fig. 1B). No animals in the control group (ND) displayed any unique phenotypes; new tissue arising in controls consistently presented as darkened, slender spikes.

MDT exposure increased bone growth and remodeling after hindlimb amputation

To characterize the internal structure of regenerates, we analyzed skeletal growth and patterning. 3D micro-CT scans obtained at 18 mpa in the MDT group revealed significantly more bone growth from the amputation plane compared to ND (Fig. 1D). Notably, interruption of the continuous bone growth from the amputation plate was observed in all MDT-exposed animals regardless of their gross anatomical patterning (Fig. 1D, yellow arrow). This interruption of continuous bone growth that was observed at the endpoint analysis began forming 12 mpa, in the MDT-exposed animals, and was maintained until the endpoint, with no changes in the spacing size from months 12 to 18 (fig. S1A). The interruption was always observed at a position paralleling the intersection of the femur and distal leg bones as evidenced by comparison to the contralateral limb, which suggested that regenerative processes were self-limiting based on previously established anatomical boundaries such as joints. Similar bone fragmentation was not observed in ND or BD groups. BD animals displayed diffuse, amorphous bone growth resembling a bony callus as observed through x-ray imaging (fig. S1B, blue box). This bony callus is a common posttraumatic correlate of amputation (fig. S1, yellow arrow). To determine the complexity of the newly formed bone, we analyzed anatomical characteristics such as bone volume ($F = 3.67$, $P < 0.05$) and trabecular density ($F = 5.12$, $P < 0.01$). MDT-treated animals displayed significantly greater bone volume and trabecular density compared to other groups. (Fig. 1, E and F). Examining the surface features of the newly formed bone revealed in MDT animals and not ND or BD animals detailed patterned topographies similar to the uncut, contralateral bone including ridges and depressions that are used as anchor points for muscle and connective tissue (Fig. 1G, indicated by arrows). The unique regenerative sequelae associated with the MDT-exposed animals were supported by longitudinal measures of bone, which displayed a sustained growth periods over the 18-month regenerative period. Repeated x-ray imaging revealed that the MDT-treated animals displayed increased bone length relative to other conditions beginning as early as 4 mpa ($P < 0.05$; Fig. 1H and fig. S1). These observations together demonstrate that the MDT treatment, delivered to the wound site for only 24 hours, induced significant bone regrowth and remodeling.

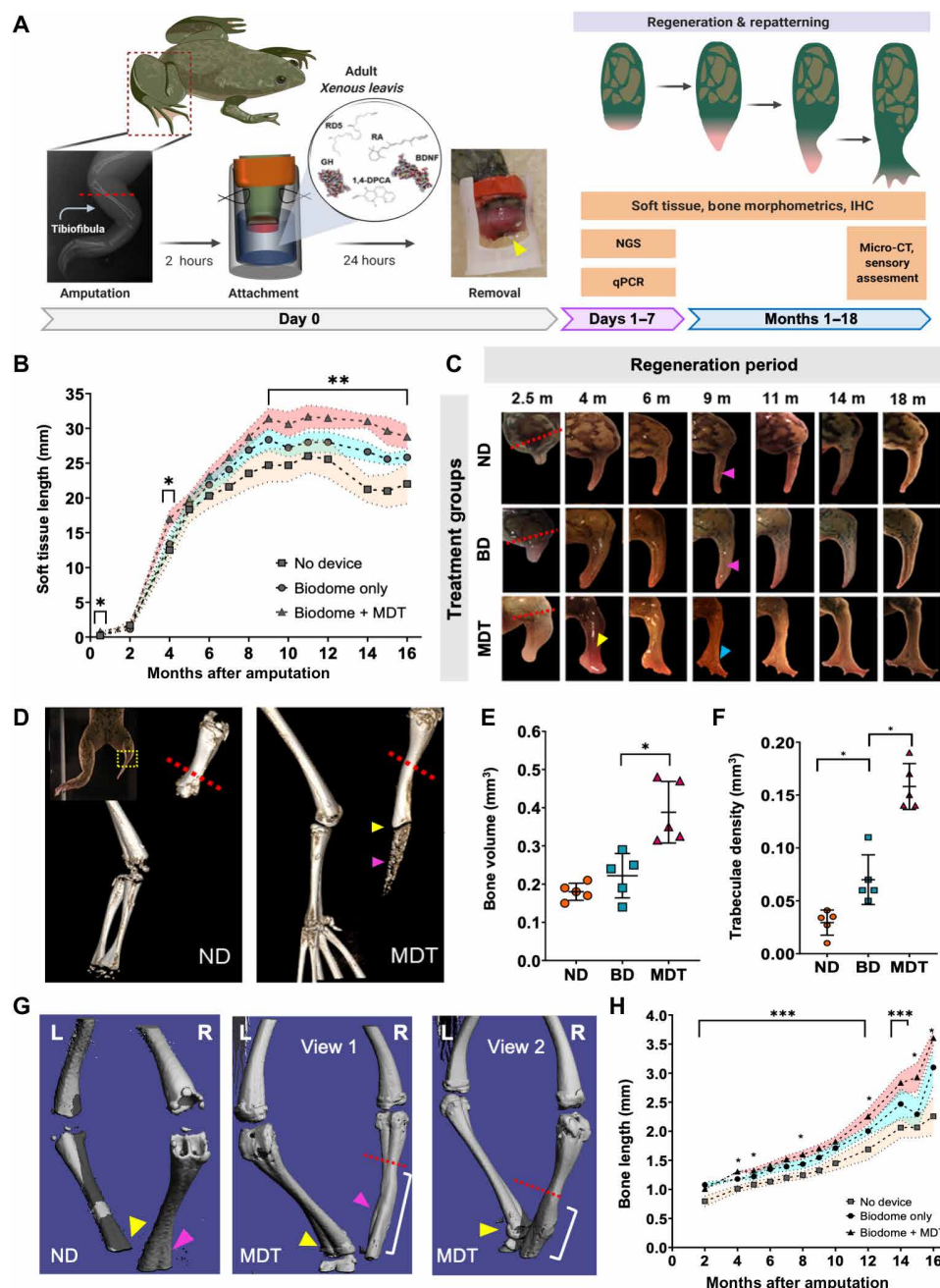


Fig. 1. Twenty-four-hour multidrug treatment delivered by bioreactor improves repatterning in regenerates. (A) *Xenopus* hindlimbs were amputated and inserted into silk-based hydrogel devices (yellow arrow) for 24 hours. Hydrogels contained a multidrug treatment (MDT) or no added factors (BD). Some animals received no device (ND). (B) Regenerated MDT hindlimbs were longer than the BD and ND groups by 2.5 mpa, as indicated by growth beyond resection site (red dashed line). At 4 mpa, vascularized structures developed at the distal extension of MDT, but not BD or ND regenerates. At 9 mpa, digit-like projections appeared (blue arrow), contrasting the hypomorphic spikes of BD and ND regenerates (pink arrows). (C) Soft tissues of MDT animals were consistently longer than BD or ND from 8 mpa [$F(2,19) = 61.9$, $P < 0.05$]. (D) Micro-CT reconstructions revealed increases in regenerate bone length (yellow arrow) and volume, as well as diffuse bone (purple arrow). (E) Volumetric quantification confirmed increased growth in MDT regenerates [$F(2,15) = 11.15$, $P < 0.001$]. (F) Tuberculae complexity increased in MDT-exposed tissue. (G) Micro-CT reconstructions show reestablishment of fine bone structures in MDT regenerates (purple arrow). (H) Longitudinal x-ray imaging indicates gradual accelerated bone growth in MDT [$F(2,19) = 31.04$, $P < 0.05$]. Means and SD are presented. * $P < 0.05$; ** $P < 0.01$; *** $P < 0.001$.

Delayed wound closure and increased blastemal markers were prominent early features of induced hindlimb regeneration within a nonregenerative system

Considering the remarkable degree of gross anatomical remodeling following MDT exposure, we sought to better understand what cellular- and tissue-level changes at early stages following amputation were associated with regenerative success. Gross anatomical observations at 0.5 weeks after treatment revealed that, after a brief hemostatic period, control animals rapidly engaged in wound closure, characterized by inward contraction of the wound tissue and

paired migration of epithelial cells—specifically, melanocytes—over the wound site (Fig. 2A). In contrast, both BD and MDT groups had significantly larger wound size diameters relative to untreated controls. Furthermore, MDT-treated animals exhibited less epithelial cell migration over the wound site and greater vascularization, as indicated by the red hue of the exposed tissue. Quantifications of the wound size diameter confirmed that MDT-treated animals displayed significantly larger wound size (2.02 ± 0.40 cm) as compared to BD (1.25 ± 0.41 cm) and ND (0.56 ± 0.17 cm; $P < 0.05$; Fig. 2B). This delay of wound closure was significantly predictive of successful

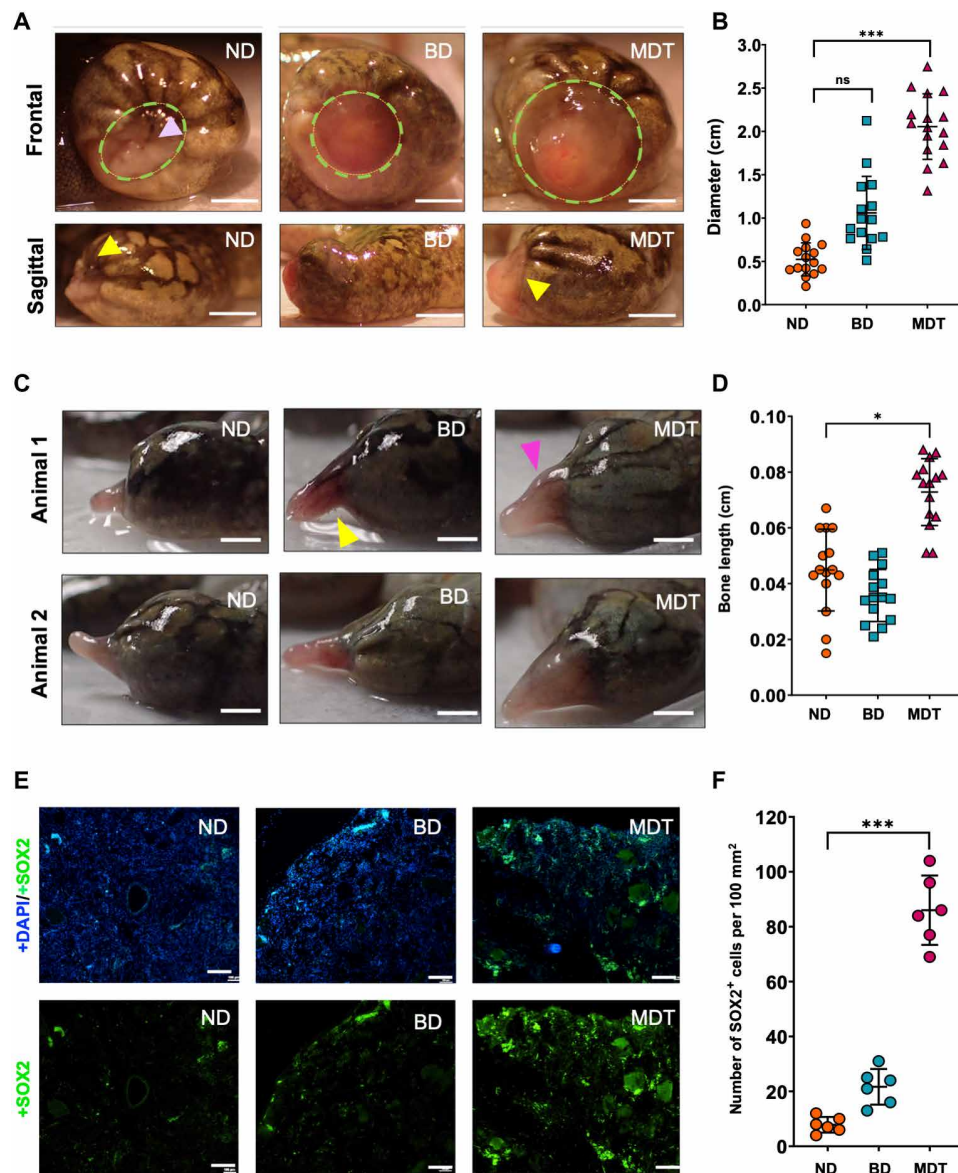


Fig. 2. MDT-exposed hindlimbs displayed wound closure delays and increased stemness markers, resulting in longer regenerates following amputation.

(A) Wound diameter (green dashed circle) 2 weeks after amputation in MDT animals as evidenced by both sagittal and frontal views. The yellow arrows indicate surgical margins, (B) revealing increased growth associated with MDT-exposed animals relative to ND animals. No significant differences were apparent when comparing BD-exposed and ND animals. ns, not significant. (C and D) SOX2 expression (green), which is a marker of stemness, was greatly increased in blastema sections of the MDT-exposed animals, while little to no expression was observed in another group (counterstained with DAPI, blue). (E) Increased soft tissue growth was also observed 2.5 mpa in the MDT-exposed group, which mirrored the (F) increased length of bone tissues as confirmed by x-ray imaging. Scale bars, 100 μ m (A, C, and E). *** $P < 0.001$.

re patterning 18 mpa [$r(28) = 0.78$; $P < 0.01$, two-tailed], with animals who had the largest wound site at 0.5 mpa showing the most growth and re patterning at 18 mpa.

Delayed wound closure was not the only early difference in the MDT group as compared to BD and ND. Macroscopic soft tissue and bone analysis at 2.5 mpa revealed thicker tissue buds displaying early signs of pigmentation and morphological complexity in the MDT, unlike the outgrowths of control animals, which only displayed slender, pale buds (Fig. 2C). A number of studies identify the cells of the dermis as integral to the formation of the blastema, contributing to different regenerated tissues such as vascular and neuronal innervation, and for organizing the overall regenerated limb pattern (46, 47). Furthermore, increased pigmentation suggests activation of pathways upstream of melanocyte differentiation like Wnt, of which we also observed changes (discussed elsewhere). Both BD- and MDT-treated groups maintained the reddened tissue color that was also observed at the wound site 2 weeks after amputation. Notably, there was no statistically significant difference between bone length when comparing ND and BD (Fig. 2D). However, x-ray analysis of the tissue revealed a significantly greater bone growth for MDT-treated animals relative to untreated controls ($P < 0.05$; fig. S1A), indicating that early patterning and growth differences are likely kickstarted by the multidrug cocktail.

Many regeneration-competent organisms, such as tadpoles, zebrafish, and axolotls, are successful whole tissue regenerators partly due to the presence or activation of pluripotent blastemal cells at the site of regeneration (10, 48). We hypothesized that the larger wound site would provide a larger blastema, or greater density of blastemal cells, which would increase the capacity for more complexity and tissue patterning downstream. We therefore assessed the presence of blastema proliferation in tissue obtained 0.5 mpa (Fig. 2E) by measuring SOX2 levels, a known marker of blastema formation (48). While untreated controls scarcely displayed positive SOX2 expression (13.2 ± 7.8), MDT-exposed animals displayed over sixfold more SOX2-positive cells (88.6 ± 12.5) (Fig. 2F). BD animals did not show a significant increase in SOX2-positive cells relative to ND, indicating that the drugs in the MDT were primarily responsible for the increased proliferation rate in treated animals.

Thus, we observed early morphological and patterning changes that indicated delayed wound closure in combination with accelerated growth and proliferation in the MDT group. This combination of outcomes in the MDT group correlated with improved outcomes at 18 mpa, indicating that the MDT treatment, while brief, provided important early cues that initiate growth programs at the amputation site.

Transcriptomic analysis of early blastemal tissue indicated developmental pathway regulation

To gain mechanistic insight into the effects of MDT exposure, we performed transcriptomic analysis of early tissue buds from MDT animals as compared to ND. Bulk RNA sequencing (RNA-seq) was used to compare the transcriptomes within blastemal cells obtained from MDT-exposed and untreated animals at 11 hpa, 24 hpa, and 7 dpa (days post-amputation) (Fig. 3A). A bioinformatics approach was then used to identify significant clusters of gene expression underlying parallel biomolecular processes governing regeneration. The number of differentially expressed genes was determined after correcting P values for multiple comparisons. The Q value was set to a FDR of 0.05, at which point genes were considered to have passed the significant threshold and to be those showing a log fold change

of 2. In examining the transcriptomic profiles of ND and MTD blastema, there were significant dynamic changes in gene expression profiles in tissues obtained at 11 hpa compared to 7 dpa, regardless of treatment (Fig. 3B). While the ND group appeared to have its highest up-regulation of expression levels at 24 hours, the MDT group showed more global down-regulation at early time points and increased gene expression at 7 days. This difference in gene expression dynamics is interesting and perhaps indicates a change in the response of the tissue at the amputation site when exposed to the MDT.

Next, we increased the resolution of our analysis by setting the FDR to \log_3 and conducted a gene enrichment analysis using KEGG pathway databases, which identify classes of genes that showed notable differences in the profiles of biological processes. Comparing the MDT and ND datasets, we then isolated the top 15 enriched up-regulated (Fig. 3C) and down-regulated (Fig. 3D) KEGG pathways, noting that the greatest number of genes undergoing change emerged 24 hpa (up, $n = 1331$; down, $n = 1098$). In addition, we found that soon after amputation (11 hpa), there were many more genes involved in metabolic regulation when comparing the MDT group and untreated controls. The metabolic signature of pro-regenerative conditions in MDT resolved by 7 dpa and was replaced by pathways associated with general cellular maintenance.

Examining each time point more closely, gene set enrichment analysis (GSEA) revealed that the top 15 highly up-regulated genes within blastemal tissues were related to neural regulation, inflammatory signaling, and cell morphogenesis (Fig. 3, E to G). Further investigation into the gene sets associated with neural-specific activation showed that expression of brain-specific kinases, neuropeptide FF, D1C dopamine receptor, and neuroligin peaked at 11 hpa before showing a decrease at 24 hpa and 7 dpa. It was also interesting to observe that Wnt7a, a gene involved in embryonic development of the anterior-posterior axis, was up-regulated at 11 hpa and subsequently further increased by 7 dpa. Conversely, the major gene sets that were down-regulated were predominantly associated with muscle structure (myosin-4, microfibril-associated glycoprotein) and metabolism (e.g., sarcosine). Crucial pro-regenerative inflammatory genes such as TGFB, PTGS2 (11 hours), and IL1B and FOXP2 (24 hours) were highly expressed at 11 and 24 hours, respectively, but gone at 7 days. Markers of morphogenesis MMP9 and SOX2 were also elevated 24 hpa.

Early MDT exposure tissue buds displayed transcriptional regulation linked with inflammation, morphogenesis, and development

An assessment of the GO terms for biological process associated transcriptional changes revealed enrichment for transcriptional processes linked with immune regulation, morphogenesis, and development. GSEA of early tissue buds (>2-fold; FDR < 0.05; MDT versus ND) revealed a significant enrichment in the morphogenetic and embryonic development signaling pathways, Notch, hedgehog, and Wnt (Fig. 4A). Pro-inflammatory signaling through TGF- β was also significantly increased in MDT relative to ND. TGF- β 1 was up-regulated within the first 24 hours after treatment ($\log_{FC} = 1.82$), indicating an early profibrotic response associated with wound closure. TGF- β 1 and TGF- β 2—which are both generally profibrotic—were significantly down-regulated at 7 dpa in MDT relative to ND ($\log_{FC} = -0.146$ and -1.83 , respectively), which indicated a net anti-fibrotic effect that parallels dynamic responses associated with the “extracellular matrix” GO set (Fig. 5C), where we observed

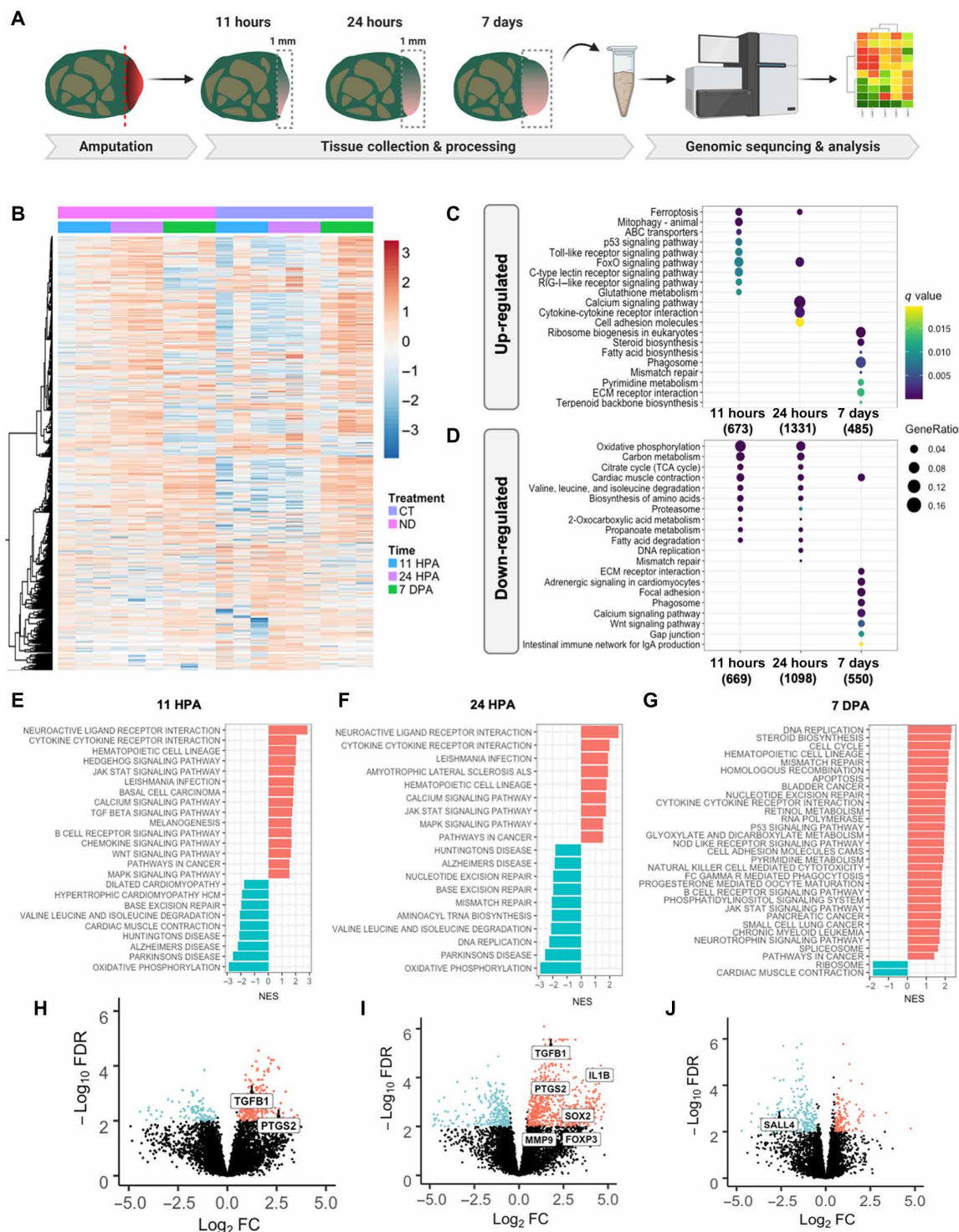


Fig. 3. Transcriptomic analysis of early wound tissue reveals gene expression changes associated with regenerative outcomes. (A) Tissue was collected from the amputation site from MDT and ND animals at 11 hpa, 24 hpa, and 7 dpa and subjected to RNA-seq analysis. (B) Heatmap comparing gene expression levels of MDT animals compared to ND shows significant differential gene expression at 11 hpa that persists to 24 hpa (see color-coded legend). At 7 dpa, however, dynamic gene expression levels return to normal, indicating a period of dynamic gene expression within 24 hours of amputation. Next, we compared the top 20 enriched (C) up-regulated and (D) down-regulated KEGG pathways in *X. laevis* treated with MDT versus ND overtime. (E and F) Gene set enrichment analysis (GSEA) revealed that inflammatory signaling and cell morphogenesis gene sets were up-regulated in blastema treated with CT at 11 hpa (left) and 24 hpa (middle) (G), which switched to more cellular regulation and metabolic mechanisms at 7 dpa (right). (H to J) We identified a handful of genes that were highly regulated in MDT blastema at 11 hpa (left), 24 hpa (middle), and 7 dpa (right)—particularly with MDT animals as compared to ND animals. Up-regulated genes included immune system-related transcripts (e.g., PTGS2, TGFB1, IL1B, and FOXP3), which suggest an important role of inflammation in pro-regenerative states.



down-regulation of COL1-2A and ADAM family genes 7 dpa despite immediate early up-regulations at 11 and 24 hpa. Together, the data indicate a shift from pro- to antifibrotic activity in MDT relative to ND, which provides one path for future studies. The significant increase in the expression of these gene sets within the first 24 hours and a nonsignificant difference at 7 dpa within hedgehog and WNT strongly suggested that the repairing epithelium represents a key stage that can induce regeneration. Genes within the Notch signaling pathway were significantly regulated on the 7th-day observational window. To further substantiate this observation, we assessed the top differentially expressed genes within these significant signaling pathways.

Among the most important, temporally ordered factors associated with successful regeneration is the orchestration of pro-regenerative immune-mediated tissue healing processes, which follow predictable, sequential patterns. First, it is necessary that pro-inflammatory cells are recruited to the site of the injury to bolster host defense and to phagocytose necrotic tissues—a major correlate of interleukin-10 (IL-10), FOXP3, and HMOX1Kit expression, of which we observed up-regulation within the first 24 hours following MDT exposure. We also observed down-regulation of genes associated with ECM deposition. Next, pro-inflammatory responses were expected to dampen as immune cells became activated, which was indicated by increased phosphatidylinositol 3-kinase (PI3K) signaling by 7 days after treatment. Pro-regenerative gene expression became increased at 24 hours including those related to cellular reprogramming, differentiation, self-renewal, survival, and proliferation: SOX2, SOX11, SALL3/4, notch1, and WNT11 (which were maintained for at least 7 days after treatment). Other key factors associated with regeneration such as FGF6, FGF3, and FGF2 were significantly regulated throughout the 7-day window (Fig. 4B). To place these dynamics in a broader context of multitissue patterning events, we then conducted network analyses.

Regenerated limbs were histologically complex, with increased innervation, endothelial growth, and connective tissue formation

To identify the overarching processes regulated by MDT exposure, we assessed the systems-level functionality of genes by coexpression gene network analyses. Coexpression analysis identified four gene modules across the control and cocktail-treated groups at 11 hours, 24 hours, and 7 days after limb amputation (Fig. 5, A and B). These modules represent categories of genes that are coexpressed across time and condition. In the untreated ND group, we identified enrichment of genes involved in ECM and collagen formation pathways (module 1; Fig. 5A), suggesting the activation of fibrotic scarring processes known to contribute to poor regeneration after trauma (Han *et al.*, 2019). The MDT group exhibited a distinct transcriptional program, characterized by activation of gene modules involved in cellular communication, muscle function, and glucose metabolism (modules 2 to 4; Fig. 5A). Induction of those large-scale functions is necessary to initiate skeletal repatterning, muscle growth, and vascularization required for complete limb regeneration (Shyh-Chang *et al.*, 2013; McCusker and Vieira, 2019; De Micheli *et al.*, 2020). Modules 2 to 4 were significantly enriched ($P < 0.00024$) in MDT-treated blastema across all time points (Fig. 5B), suggesting that animals receiving the pro-regenerative MDT had sustained up-regulation of those genes associated with cell communication, myogenesis, and glucose metabolism. In contrast, these modules were significantly repressed ($P < 0.012$) in ND groups at all time

points assessed (Fig. 5B). Critical genes involved with ECM remodeling, such as those in the ADAM family (ADAMTS1, ADAMTS5, and ADAMTS9), were significantly increased within 24 hours after MDT exposure and decreased 7 dpa (Fig. 5C). ADAM proteins play an important role in regeneration, as their activation induces the activation of muscle satellite cells to induce muscle regeneration after injury in mice. We observe that this same gene, ADAMTS1, was significantly up-regulated in MDT animals within 11 to 24 hours (Fig. 5C). However, at the 7-day time point, module 2—genes involved in cellular communication—was significantly up-regulated ($P = 0.00074$) in the same untreated group, suggesting that there was little difference in the enrichment of cell-cell communication pathways between the treated and untreated groups 1 week after amputation.

To confirm changes to the histoarchitecture of regenerates, we assayed markers of laminin, SMA, and fibronectin to assess vascularization and connective tissue formation. SMA and laminin expression at 18 mpa were compared across conditions (Fig. 5E). The number of blood vessels identified in each section was significantly greater in the MDT-treated group as compared to both the BioDome only and ND groups [$H(19.84) = P < 0.001$; Fig. 5C], indicating that the MDT facilitates vascularization of the regenerate, more than doubling the number of blood vessels in the MDT-treated regenerate relative to untreated controls. Fibronectin expression within MDT regenerates was also significantly increased relative to other groups (Fig. 5D). Increased particle complexity in the MDT-treated regenerate reflected a unique microanatomical (structural) complexity that was not observed for other groups (Fig. 5D). Consistent with bone and soft tissue patterning, the 24-hour MDT group displayed increased particle complexity relative to both the BioDome only and ND groups (Fig. 5D), indicating that the MDT itself likely facilitated growth of cartilage and connective tissues in the regenerate.

Peripheral nerve regeneration and functional recovery of sensorimotor ability after MDT exposure

Hindlimbs facilitate behaviors vital to an animal's survival; it is critical to identify interventions that facilitate recovery of functionality, not just anatomy. We therefore investigated regenerate functionality by assessing sensorimotor response in adult *X. laevis* animals 18 mpa and treatment. To determine the presence of neural tissues, we conducted immunohistochemical analyses to assess peripheral nerve regeneration and reinnervation. Reinnervation, as measured by AAT staining, revealed a significant increase in the number of AAT⁺ nerve bundles within MDT animals compared to either ND or BD groups ($U = 13$, $P = 0.0014$; Fig. 6A). The number of AAT⁺ bundles was comparable when comparing the ND and BD groups, indicating that the MDT treatment influenced nerve bundle regrowth and innervation of the regenerate. Not only were there more bundles in the MDT-exposed animals, but these animals also exhibited significantly larger AAT bundle diameters relative to the ND group (Fig. 6C). Again, there was no significant increase in bundle size between the BD and ND groups, indicating that reinnervation is driven primarily by the MDT drugs, not the bioreactor.

Next, to assess whether the 18-mpa regenerates regained function, a sensorimotor assessment was conducted (Fig. 6D). Using standardized VF filaments (minimum force: 0.008g; maximum force: 300g), the regenerated right hindlimb was probed at the most distal end with filaments of increasing pressure. The first filament that induced a clear response (movement from the stationary position) determined

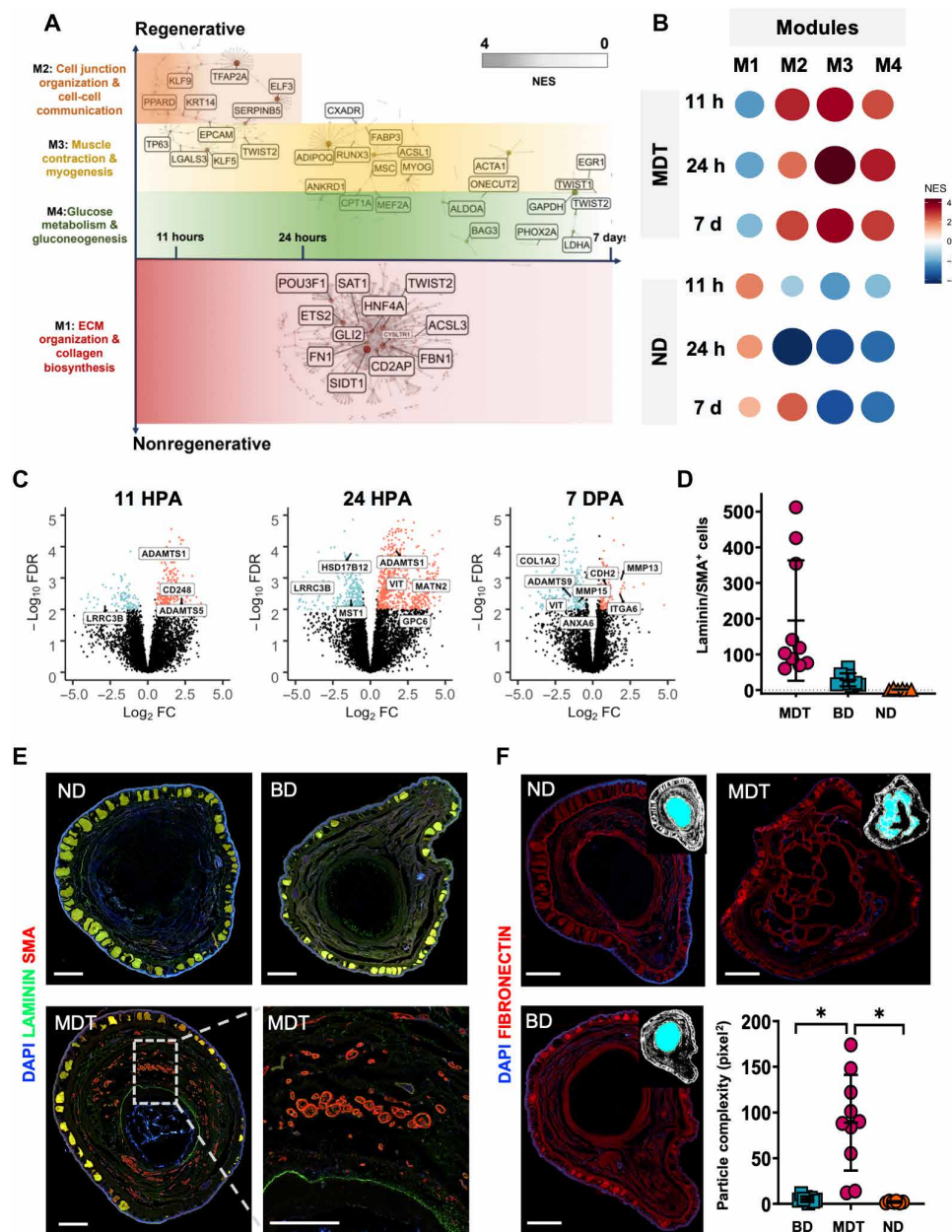


Fig. 5. GSEA revealed four distinct expression modules indicative of complex tissue repatterning. CEMiTool was used to identify covarying gene sets as a function of high fold changes in the MDT (CT) and ND animals, yielding modules M1 to M4. (A) Relative expression of modules between time points and conditions (dark red circles = up-regulation; dark blue circles = down-regulation). (B) M2 to M4 were up-regulated in MDT animals versus ND across all time points, peaking at 24 hpa; however, M1 was down-regulated in the MDT condition, most highly at 11 hpa, and decreasing to 7 dpa. M3 genes were up-regulated in MDT relative to ND including acetylcholine activity and muscle activation. M4 genes were up-regulated in MDT relative to ND including glucose metabolism. (C) GO data within the ECM development pathway indicated up-regulation of ADAM family genes at 11 and 24 hpa; however, they were down-regulated at 7 dpa. (D and E) Cross-sectioned regenerates (18 mpa) were double fluorescent-stained for markers of vascularization: smooth muscle actin (red) and basement membrane (green). SMA/laminin⁺ bundles were increased in MDT animals relative to device only or ND groups ($P < 0.001$). (F) Fibronectin⁺ cartilaginous cores of regenerates displayed increased structural complexity associated with the MDT group relative to all other groups ($*P < 0.05$). Scale bars, 1 mm. Means and SD are presented.

the response threshold, which was recorded. Behavioral assays were averaged over 2 days. We observed that all MDT-treated hindlimb regenerates displayed comparable stimulus-response patterns to the ND group ($P > 0.01$; Fig. 6E), indicating that they had regained significant reinnervation and neuromuscular reintegration compared to normal functionality preinjury, regardless of the soft tissue

patterning complexity. In the BD group, responses varied markedly between individual animals, with a subset of animals performing at near-normal levels and a subset that was unable to detect the stimulus ($56.6 \pm 98.8\text{g}$), while untreated control animals reliably failed to display any response to applications of force at any value up to and including 300g (Fig. 6E), indicating profound loss of function. The

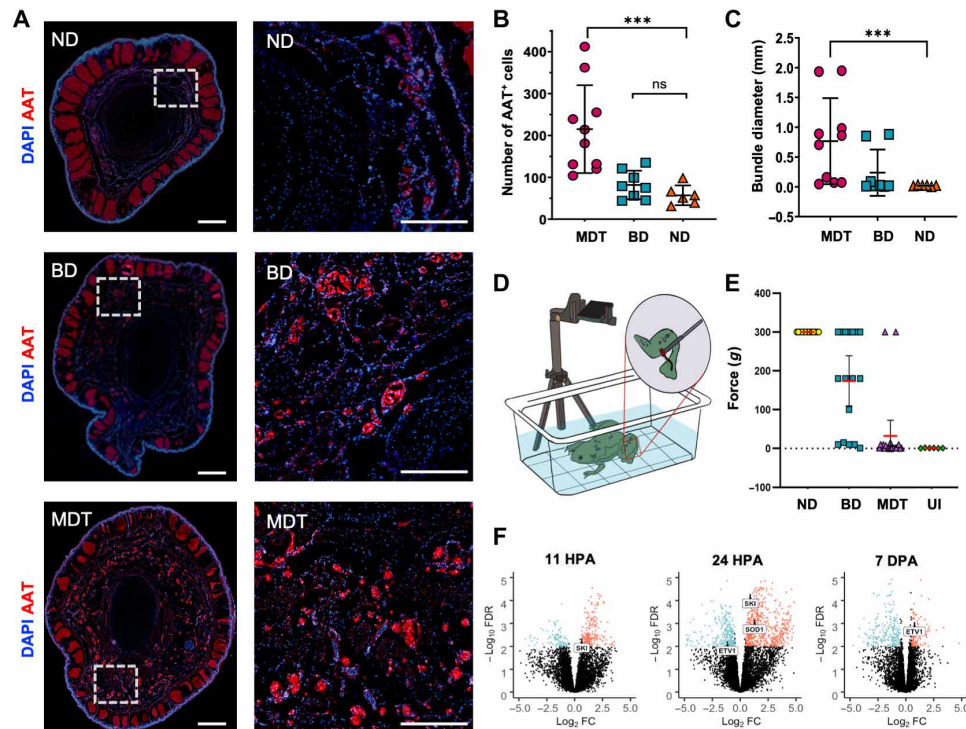


Fig. 6. Nerve regeneration and sensorimotor reintegration in MDT-exposed animals are associated with gain of function in regenerated hindlimbs. (A) Distal (left column) and proximal (right column) sections of the regenerates were labeled with antibodies for an axonal nerve marker, AAT (red), and counterstained with DAPI (blue). Sections obtained from regenerates exposed to the MDT immediately after amputation displayed significantly more AAT⁺ bundles (B) [$N = 10$ MDT, $n = 8$ BD, $n = 6$ ND, Kruskal-Wallis $H(3,24) = 15.12$, $P < 0.005$] with wider diameter (C) [Mann-Whitney $U(3,24) = 11.74$, $P = 0.0028$] than those sections obtained from ND or BD-exposed animals. (D) Sensorimotor reintegration as assessed by VF filaments applied to the distal tip of the regenerate showed gain of function in the MDT group similar to that of unamputated (wild-type) limbs from ND animals. (E) MDT animals displayed a reliable restoration of sensorimotor function as evidenced by a stimulation force threshold (0g) matching uninjured (UI) animals ($P > 0.05$). BD animal sensorimotor function was highly variable, with subsets displaying a complete lack of response (top cluster), a partial response (middle cluster), or full restoration of function (bottom cluster). ND animals universally displayed a total lack of response to stimulation. (F) SKI gene expression, which is associated with peripheral myelination and glial cell proliferation, was up-regulated at 11 and 24 hpa but not at 7 dpa. ETV1 gene expression, which is associated with the peripheral glial repair response to injury, was down-regulated at 24 hpa and later up-regulated at 7 dpa. Means and SD are presented. *** $P < 0.001$.

recovery of responsiveness in the MDT-treated group and some of the BD group indicates that, at a minimum, the bioreactor device alone provides effective support to peripheral nerves and facilitates reinnervation of tissues with time, and that the device with the MDT further enhanced regeneration.

Evidence for reinnervation was one of the most profound effects we observed in this study. Not only was it easily observable through immunohistochemical analysis, but also GO pathway and analyses revealed peripheral nerve regeneration as one of the main pathways that were significantly enriched in early blastema tissues. Specifically, the analysis indicated that differential gene expression related to neural cell development and maintenance was observed, with many genes up-regulated within 24 hours of amputation, and a marked down-regulation of those genes by 7 dpa (Fig. 6F). Levels of SKI expression [a gene associated with Schwann cell proliferation and myelination (49)] were significantly up-regulated 11 and 24 hpa in tissue that was MDT-exposed compared to untreated tissue. ETV1 gene expression, which is associated with Schwann cell repair response following injury (50), was also differentially expressed over time, beginning with down-regulation at 24 hours and later switching to up-regulation by 7 dpa. This is of particular interest because transcription factor ETV1, which is a downstream effector of mitogen-activated protein kinase kinase (MEK)/extracellular signal-regulated

kinase (ERK) signaling is also involved in Schwann cell repair response following injury (51). Together, these findings show that a brief 24-hour exposure to the MDT-loaded device induced early transcriptional changes in peripheral nerve regulation that may contribute to peripheral nerve regeneration and functional recovery in otherwise nonregenerative adult animals.

DISCUSSION

Restoring form and function after limb loss in nonregenerative species, while avoiding neoplastic conversion, represents a complex task that demands appropriate wound management, regulation of inflammation, induction of growth, promotion of tissue repatterning, and a cessation of growth and remodeling at the appropriate time. The remarkable complexity of functional limbs suggests that the fastest path toward this goal may lie in triggering native, self-limiting modules of organogenesis, not continuous micromanagement of the lengthy process at the cell and molecular levels. We hypothesized that kickstarting a limb-building routine required two components acting at a very early initiating stage of the process: first, an enclosed and permissive microenvironment that enables the wound cells to control the biochemical milieu following injury and, second, an instructive set of signals that specifically trigger a limb-building program.

We implemented this via a short exposure of limb amputation wounds to a wearable bioreactor containing a payload of five select biochemical factors (MDT).

Our MDT system consists of five small-molecule compounds (BDNF, GH, 1,4-DPCA, RD5, and RA), which, in previous studies, have been independently shown to have marked pro-regenerative effects. One unique aspect of the study was to coordinate the simultaneous delivery of a multifactorial treatment using a controlled-release mechanism intrinsic to the silk-biomaterial bioreactor system. Several injury and lesion studies have shown that delivery of exogenous BDNF to nonregenerative rodents increased the number of dorsal root ganglion (DRG) neurons and peripheral axon and promoted recovery of motor functions (52, 53)—findings that are congruent with our demonstrated effects on nervous tissues. In axolotls, hypophysectomy studies have shown the importance of GH to limb regeneration, in that supplementation of GH restored the speed and ability to regenerate limbs in animals without a pituitary (54). Suppression of fibrotic pathways is critical for successful regeneration. 1,4-DPCA, a selective and potent inhibitor of prolyl 4-hydroxylase, inhibits excessive collagen deposition, which is a classic feature of fibrosis and inducer of proangiogenic processes (55, 56), hypoxia-inducible factor-1 α (HIF-1 α) modulations, which are known to be vital in maintaining appropriate oxygen content within regenerative tissue microenvironments (57). It is very clear that tipping the scales of inflammation can either hinder or promote limb regeneration and a fine control of this balance can turn a nonregenerative animal into a regenerative one. RD5 is a member of the resolvins family, which is docosahexaenoic acid (DHA)-derived. In addition to inducing anti-inflammatory responses, RD5 promoted the resolution of an existing inflammatory response back to a noninflamed state (58). RA, a metabolite of vitamin A, is as a well-known morphogen, and its role in vertebrate limb development and regeneration has been well established (59).

We found that a brief (24-hour) exposure to this MDT delivered by wearable bioreactor resulted in a remarkable limb regenerative response lasting over 1 year. We also observed long-term growth and significant tissue repatterning that was self-sustaining. The brief intervention had long-term consequences, potentiating temporally complex gene expression and de novo tissue formation including reinnervation that successfully reestablished sensorimotor function. Our collective data suggest that early targeted interventions may shift the burden of regeneration to the limb itself, sidestepping reliance on longer-term therapeutic strategies like the use of stem cells, serialized treatments, and other means of persistent micromanagement of restorative growth and patterning.

Treatment effects were apparent as early as 2 weeks after amputation, where wound closure was significantly affected by the multi-drug exposure (Fig. 2, A and B). This macroscale phenomenon was complemented by several key molecular events, which, together, reestablished the microenvironmental conditions to induce local morphogenetic control. Gene expression profiles were profoundly influenced by the MDT, with early up-regulation of wound-managing inflammatory and morphogenic signaling that later switched to maintenance-based control over cell regulation and metabolism (Fig. 3, B to J). The temporal specificity of gene expression was notable, where morphogens and key regulators such as Wnt, hedgehog, TGF- β , and Notch were progressively activated within the first 7 dpa (Fig. 4, A and B). Tissues associated with multidrug-treated animals displayed early SOX2 expression (Fig. 2, C and D) and, later,

reestablished vasculature (Fig. 5E) and nerve (AAT; Fig. 6, A to C). Furthermore, the presence of nerve bundles (Fig. 6C) rather than a disintegrated phenotype in untreated controls (ND) indicated that active patterning was occurring. Superficial features were impressive, including the presence of pseudo-digits (Fig. 1C), which have not been previously shown to regenerate in adult nonregenerative systems. Also notable was the appearance of anatomical detail observed in regenerated bone including functionally relevant sulci as measured by micro-CT (Fig. 1G). That bone growth was initiated by treatment but later self-inhibited at regions equivalent to contralateral joints was particularly interesting. Our results suggest a dynamic mobilization of both osteoblasts and osteoclasts to grow and sculpt bone structures. These findings suggest that tissues were patterned toward particular end states rather than progressing haphazardly, ultimately scaling the newly formed bone appropriately.

Consistent with considerable structural restoration was the reliable reintegration of neuromuscular tissues sufficient to elicit robust kicking responses when stimulated by mechanical probes. For most MDT animals, sensorimotor integrity was indistinguishable from animals that were never amputated (Fig. 6E). This gain-of-function result was particularly encouraging, as it points to the MDT restoring function in the newly regenerated limb. In addition to their reported stimulus-response patterns, we regularly observed these animals using their limbs to self-orient, swim toward food, and avoid auditory or mechanical disturbances near their tanks. While there is certainly room to improve the regeneration of digits, webbing, and other distal limb features, these complex regenerates were sufficient to provide additional functional capacities that were not apparent in the hypomorphic spikes formed in place of amputated limbs in untreated animals.

In many cases, the wearable bioreactor alone produced a significant regenerative response, albeit to a lesser degree of limb structure and function relative to the infused, MDT condition. While paddle and pseudo-digit formations were not observed in animals exposed to only BD, it was evident that many measures were significantly affected including soft tissue length (Fig. 1B), trabeculae density (Fig. 1F), bone length (Fig. 1H), wound diameter at 0.5 mpa (Fig. 2A), AAT expression (Fig. 6A), and the restoration of sensorimotor function as inferred by VF tests (Fig. 6E). One potential explanation is the BioDome-wound interface itself. The brief 24-hour period during which the silk-based hydrogel interfaced with the wound site may have facilitated paracrine signaling at the stump by maintaining local concentration gradients while providing a bulwark against effects of fluid shear and any undesirable consequence of a wound freely exposed to water surrounding the animal. Furthermore, subtle mechanical cues at the wound-hydrogel interface may also stimulate some of these features. As anticipated, the controlled microenvironment of the BD alone induced a partial limb-building routine (or prevented its normative inhibition); however, adding instructive signals associated with the MDT condition amplified the effects markedly.

While the complex process of limb regeneration is not fully understood, it is evident that it is the early events of wound healing and dedifferentiation that distinguish the amphibian from the mammalian response. Amputation of the mature limb transects a number of distinct tissues, including the dermis, muscle, nerve, blood vessels, and bone, as well as the loose connective tissue that surrounds them, thus exposing all of these tissues at the wound surface. In urodeles, the initial response to the injury is the formation of a fibrin clot that covers the wound surface and provides a substrate on which peripheral epidermal cells migrate to close the wound (60). This response

is fast, where in urodeles a wound can be completely closed within 12 hours. By comparison to a size-matched mammalian wound, such as an amputated mouse digit that takes multiple days-months to close, the speed of urodele wound closure is extraordinary. Wound cells in mammals, which experience dry air and contact with the ground, have been selected for a scarring response that minimizes infection and blood loss, given that pro-regenerative injury currents (61) cannot exist in a nonaqueous external milieu, and moreover, the unprotected environment is unlikely to support regeneration and patterning of a blastema. By contrast, some of the outcomes of rapid wound closure include minimizing tissue damage, minimizing infection and an inflammation response, and rapid stabilization of the wound microenvironment. Therefore, interventions such as the BD, which provide a controlled interface at the wound site, may represent one way to overcome the time constant of species' wound-closure response, mimicking one of the advantageous properties of urodele regeneration. The results presented here are encouraging; however, physiological differences across species suggest that a number of important steps remain for the extrapolation of these data to mammals.

Following amputation of the limb, the early 24-hour window point is critical, not only for wound closure but also for the transformation of the wound epithelium into a specialized structure called the apical epithelial cap (AEC) that is required for limb outgrowth, the migration of dedifferentiated cells to the center of the wound where a blastema forms, and the proliferation of blastema cells (62). Signatures of this specialized AEC formation, found within the wound epidermis, is absent in nonregenerative animals such as birds, adult mice, and adult frogs (63). Several studies have shown that young *Xenopus* limb buds that are able to regenerate express several fibroblast-specific genes after amputation, and that a lack of these expressions, as observed in knockout studies, prevents limb regrowth. Since then, several investigators have shown that adult *Xenopus* lack these FGF genes as they age (64). Our MDT-exposed animals displayed increased expression of FGF2, FGF6, and FGF8 within 11 hpa, which was maintained 7 days later (Fig. 4B). This antifibrosis phenomenon is also supported by a down-regulation of fibrosis-associated genes such as COLA1, Twist 2, ACSL3, and FBN1 (Fig. 5, A and B) in a time-dependent manner, whereby most of the genes related to ECM remodeling are differentially expressed 7 dpa (fig. S2, A, E, and F).

Postmetamorphic *Xenopus* limbs display a hypomorphic regenerative response that involves blastema formation; however, they face multiple regeneration barriers such as an absence of Shh reexpression by posterior mesenchymal cells (65). We have strong evidence to show that our MDT-exposed animals increased their hedgehog signaling within the first 24 hours, leveling off by day 7 post-amputation (Fig. 4C) as evidenced by fold change values for the *shh* gene at 11 hours (4.74), 24 hours (7.25), and 7 days (2.41). We also observed an up-regulation of SOX transcription factors that are meant to signal increased stem cell differentiation and renewal in our RNA-seq, which we validated a month later at the protein expression level (Fig. 2, E and F). Together, the findings indicate that one or more factors associated with the MDT exposure increased morphological plasticity by inducing gene expression critical to tissue repatterning. One outstanding question relates to possible epigenetic modifications associated with the reported dynamic changes to metabolic pathways across experimental groups. DNA methylation and histone modification are known to play an important role in cellular plasticity following injury including reprogramming to

achieve pro-regenerative cell fates. The degree to which the intrinsic conditions of the BioDome and the MDT are affecting epigenetic mechanisms represents one important future direction.

A clear roadmap to limb or appendage regeneration was built on the shoulders of injury studies that have shown that dormant regenerative potential can be activated by targeted treatment with specific morphogenetic agents. While genomic studies of specific developmental or regeneration-specific genes have yielded great insight into the reasons why regenerative competence is expressed, scaling to humans has proved difficult without micromanaging the system. Recent works have demonstrated interesting effects from the exogenous applications of morphogens (e.g., BMPs and FGFs) (25, 66–72) or even stem cells in mammalian digit regeneration (73, 74). Even in studies where a whole limb amputation and treatment were tested using a unique bioelectric approach, a fully functional limb was not observed (4), although considerable molecular dynamics and some tissue growth were observed. In our previous work with exogenous applications of progesterone to adult *Xenopus*, we did not observe the level of patterning and functional recovery reported here—which represents an important step forward and a proof-of-principle demonstration of the multidelivery approach to full limb regeneration and functional restoration. While the current state of progress is encouraging, the aforementioned mammalian studies were conducted in either mammalian systems at the boundary of regeneration competence or successfully regenerated small tissues such as joints or bones.

There are several outstanding questions to guide future work. One variable requiring additional systematic analysis in this highly tractable model is the duration of bioreactor application. Intervention latency, exposure duration, and intermittent schedules of application may yield alternative outcomes. In addition, a number of new ingredients should be assayed—especially bioelectric triggers that have previously shown promise in froglet limb and tail models (75, 76). Of course, there are also limitations inherent to the model system. Most notably, the long period required to observe the multistage regeneration processes following the initial treatment is somewhat impractical and precluded a high-throughput screen of all possible combinations of MDT ingredients and doses. We maintained and housed some animals for over 18 months and observed inflections of growth up to 14 mpa (Fig. 1H). However, the protracted regeneration period of the postmetamorphic and largely nonregenerative *Xenopus* model is physiologically relevant as it matches mammalian capacities and time scales and provides a greater window within which to observe stage remodeling without missing relevant growth milestones. The current work represents an extremely promising starting point for experiments in clinically relevant mammalian models (77–79). It should be noted that while the lengthy regeneration time inhibits screening large numbers of intervention options, effective treatments would not be problematic when applied because even multiyear repair latencies would be worthwhile and a relatively short period of time in the life of human patients benefits from restored appendages. However, it remains unclear whether, from a biomedical perspective, the physical size of the human limb would affect the feasibility of an endogenous limb-building strategy.

The generalizability of this specific MDT must next be tested in mammals. We suggest that the overall strategy of providing wound cells with an aqueous, amniotic-like environment, which is uniquely given through our bioreactor, that contains pro-regenerative signals is likely to be an effective method for kickstarting biomedically relevant growth and patterning cascades that are too complex to directly

implement. By stimulating wound cells with an environment that resembles the embryonic context, it may be possible to offload the complexity of the regenerative process onto the system itself, triggering endogenous modules that provide a clinically relevant improvement of form and function. One additional direction that may present new opportunities for enhanced regeneration is to assess immune function in relation to tissue remodeling. It has been known for many years that immune competency and regeneration are reciprocally linked. That we observed early wound-managing inflammatory signaling could suggest that the MDT exposure was immunomodulatory; however, additional experiments are required to elucidate whether the cause-effect relationships are proximal or not. The goal of triggering latent tissue-building routines to regrow limbs in humans may be achieved by identifying and exploiting principles observed in highly regenerative organisms.

SUPPLEMENTARY MATERIALS

Supplementary material for this article is available at <https://science.org/doi/10.1126/sciadv.abj2164>

[View/request a protocol for this paper from Bio-protocol.](#)

REFERENCES AND NOTES

- K. Ziegler-Graham, E. J. MacKenzie, P. L. Ephraim, T. G. Trivison, R. Brookmeyer, Estimating the prevalence of limb loss in the United States: 2005 to 2050. *Arch. Phys. Med. Rehabil.* **89**, 422–429 (2008).
- R. B. Borgens, What is the role of naturally produced electric current in vertebrate regeneration and healing. *Int. Rev. Cytol.* **76**, 245–298 (1982).
- L. Leppik, H. Zhuhua, S. Mobini, V. Thottakkattumana Parameswaran, M. Eischen-Loges, A. Slavici, J. Helbing, L. Pindur, K. M. C. Oliveira, M. B. Bhavsar, L. Hudak, D. Henrich, J. H. Barker, Combining electrical stimulation and tissue engineering to treat large bone defects in a rat model. *Sci. Rep.* **8**, 6307 (2018).
- L. P. Leppik, D. Froemel, A. Slavici, Z. N. Ovidia, L. Hudak, D. Henrich, I. Marzi, J. H. Barker, Effects of electrical stimulation on rat limb regeneration, a new look at an old model. *Sci. Rep.* **5**, 18353 (2015).
- K. M. C. Oliveira, J. H. Barker, E. Berezikov, L. Pindur, S. Kynigopoulos, M. Eischen-Loges, Z. Han, M. B. Bhavsar, D. Henrich, L. Leppik, Electrical stimulation shifts healing/scarring towards regeneration in a rat limb amputation model. *Sci. Rep.* **9**, 11433 (2019).
- S. D. Smith, 476—The role of electrode position in the electrical induction of limb regeneration in subadult rats. *Bioelectrochem. Bioenerg.* **8**, 661–670 (1981).
- M. A. Suckow, S. L. Voytik-Harbin, L. A. Terill, S. F. Badylak, Enhanced bone regeneration using porcine small intestinal submucosa. *J. Invest. Surg.* **12**, 277–287 (1999).
- S. J. Cho, S. Y. Kim, H. C. Jeong, H. Cheong, D. Kim, S. J. Park, J. J. Choi, H. Kim, H. M. Chung, S. H. Moon, H. J. Cha, Repair of ischemic injury by pluripotent stem cell based cell therapy without teratoma through selective photosensitivity. *Stem Cell Rep.* **5**, 1067–1080 (2015).
- H. Lawall, P. Bramlage, B. Amann, Stem cell and progenitor cell therapy in peripheral artery disease. A critical appraisal. *Thromb. Haemost.* **103**, 696–709 (2010).
- G. Lin, Y. Chen, J. M. W. Slack, Imparting regenerative capacity to limbs by progenitor cell transplantation. *Dev. Cell* **24**, 41–51 (2013).
- Y. Kawakami, C. Rodriguez Esteban, M. Raya, H. Kawakami, M. Martí, I. Dubova, J. C. Izpisua Belmonte, Wnt/ β -catenin signaling regulates vertebrate limb regeneration. *Genes Dev.* **20**, 3232–3237 (2006).
- H. Yokoyama, H. Ide, K. Tamura, FGF-10 stimulates limb regeneration ability in *Xenopus laevis*. *Dev. Biol.* **233**, 72–79 (2001).
- B. D. Cox, M. H. Yun, K. D. Poss, Can laboratory model systems instruct human limb regeneration? *Development* **146**, dev181016 (2019).
- A. Joven, A. Elewa, A. Simon, Model systems for regeneration: Salamanders. *Development* **146**, dev167700 (2019).
- D. Lee-Liu, M. Moreno, L. I. Almonacid, V. S. Tapia, R. Muñoz, J. von Marées, M. Gaete, F. Melo, J. Larrain, Genome-wide expression profile of the response to spinal cord injury in *Xenopus laevis* reveals extensive differences between regenerative and non-regenerative stages. *Neural Dev.* **9**, 12 (2014).
- N. Rao, F. Song, D. Jhamb, M. Wang, D. J. Milner, N. M. Price, T. L. Belecky-Adams, M. J. Palakal, J. A. Cameron, B. Li, X. Chen, D. L. Stocum, Proteomic analysis of fibroblastoma formation in regenerating hind limbs of *Xenopus laevis* froglets and comparison to axolotl. *BMC Dev. Biol.* **14**, 32 (2014).
- G. L. Johnson, E. J. Masias, J. A. Lehoczyk, Cellular heterogeneity and lineage restriction during mouse digit tip regeneration at single-cell resolution. *Dev. Cell* **52**, 525–540 e525 (2020).
- J. L. Whited, M. Levin, Bioelectrical controls of morphogenesis: From ancient mechanisms of cell coordination to biomedical opportunities. *Curr. Opin. Genet. Dev.* **57**, 61–69 (2019).
- D. Payzin-Dogru, J. L. Whited, An integrative framework for salamander and mouse limb regeneration. *Int. J. Dev. Biol.* **62**, 393–402 (2018).
- P. Tandon, F. Conlon, J. D. Furlow, M. E. Horb, Expanding the genetic toolkit in *Xenopus*: Approaches and opportunities for human disease modeling. *Dev. Biol.* **426**, 325–335 (2017).
- A. S. Tseng, M. Levin, Tail regeneration in *Xenopus laevis* as a model for understanding tissue repair. *J. Dent. Res.* **87**, 806–816 (2008).
- C. M. Illingworth, Trapped fingers and amputated finger tips in children. *J. Pediatr. Surg.* **9**, 853–858 (1974).
- J. N. Dent, Limb regeneration in larvae and metamorphosing individuals of the South African clawed toad. *J. Morphol.* **110**, 61–77 (1962).
- K. Muneoka, G. Holler-Dinsmore, S. V. Bryant, Intrinsic control of regenerative loss in *Xenopus laevis* limbs. *J. Exp. Zool.* **240**, 47–54 (1986).
- N. Saito, K. Nishimura, A. Makanae, A. Satoh, Fgf- and Bmp-signaling regulate gill regeneration in *Ambystoma mexicanum*. *Dev. Biol.* **452**, 104–113 (2019).
- G. Lin, J. M. W. Slack, Requirement for Wnt and FGF signaling in *Xenopus* tadpole tail regeneration. *Dev. Biol.* **316**, 323–335 (2008).
- A. Satoh, A. Makanae, A. Hirata, Y. Satou, Blastema induction in aneurogenic state and Prx-1 regulation by MMPs and FGFs in *Ambystoma mexicanum* limb regeneration. *Dev. Biol.* **355**, 263–274 (2011).
- Y. Taniguchi, K. Watanabe, M. Mochii, Notochord-derived hedgehog is essential for tail regeneration in *Xenopus* tadpole. *BMC Dev. Biol.* **14**, 27 (2014).
- D. M. Ho, M. Whitman, TGF- β signaling is required for multiple processes during *Xenopus* tail regeneration. *Dev. Biol.* **315**, 203–216 (2008).
- N. R. Love, Y. Chen, S. Ishibashi, P. Kritsiligkou, R. Lea, Y. Koh, J. L. Gallop, K. Dorey, E. Amaya, Amputation-induced reactive oxygen species are required for successful *Xenopus* tadpole tail regeneration. *Nat. Cell Biol.* **15**, 222–228 (2013).
- N. Yakushiji, M. Suzuki, A. Satoh, H. Ide, K. Tamura, Effects of activation of hedgehog signaling on patterning, growth, and differentiation in *Xenopus* froglet limb regeneration. *Dev. Dyn.* **238**, 1887–1896 (2009).
- M. Suzuki, N. Yakushiji, Y. Nakada, A. Satoh, H. Ide, K. Tamura, Limb regeneration in *Xenopus laevis* froglet. *ScientificWorldJournal* **6** (suppl. 1), 26–37 (2006).
- C. Herrera-Rincon, A. S. Golding, K. M. Moran, C. Harrison, C. J. Martyniuk, J. A. Guay, J. Zaltsman, H. Caraballo, D. L. Kaplan, M. Levin, Brief local application of progesterone via a wearable bioreactor induces long-term regenerative response in adult *Xenopus* hindlimb. *Cell Rep.* **25**, 1593–1609.e7 (2018).
- A. Golding, J. A. Guay, C. Herrera-Rincon, M. Levin, D. L. Kaplan, A tunable silk hydrogel device for studying limb regeneration in adult *Xenopus laevis*. *PLOS ONE* **11**, e0155618 (2016).
- D. Hechavarria, A. Dewilde, S. Braunhut, M. Levin, D. L. Kaplan, BioDome regenerative sleeve for biochemical and biophysical stimulation of tissue regeneration. *Med. Eng. Phys.* **32**, 1065–1073 (2010).
- D. N. Rockwood, R. C. Preda, T. Yücel, X. Wang, M. L. Lovett, D. L. Kaplan, Materials fabrication from Bombyx mori silk fibroin. *Nat. Protoc.* **6**, 1612–1631 (2011).
- B. P. Partlow, C. W. Hanna, J. Rnjak-Kovacina, J. E. Moreau, M. B. Applegate, K. A. Burke, B. Marelli, A. N. Mitropoulos, F. G. Omenetto, D. L. Kaplan, Highly tunable elastomeric silk biomaterials. *Adv. Funct. Mater.* **24**, 4615–4624 (2014).
- A. Dobin, C. A. Davis, F. Schlesinger, J. Drenkow, C. Zaleski, S. Jha, P. Batut, M. Chaisson, T. R. Gingeras, STAR: Ultrafast universal RNA-seq aligner. *Bioinformatics* **29**, 15–21 (2013).
- Y. Liao, G. K. Smyth, W. Shi, featureCounts: An efficient general purpose program for assigning sequence reads to genomic features. *Bioinformatics* **30**, 923–930 (2014).
- M. D. Robinson, A. Oshlack, A scaling normalization method for differential expression analysis of RNA-seq data. *Genome Biol.* **11**, R25 (2010).
- C. W. Law, Y. Chen, W. Shi, G. K. Smyth, voom: Precision weights unlock linear model analysis tools for RNA-seq read counts. *Genome Biol.* **15**, R29 (2014).
- M. E. Ritchie, D. Diyagama, J. Neilson, R. van Laar, A. Dobrovic, A. Holloway, G. K. Smyth, Empirical array quality weights in the analysis of microarray data. *BMC Bioinformatics* **7**, 261 (2006).
- M. E. Ritchie, B. Phipson, D. Wu, Y. Hu, C. W. Law, W. Shi, G. K. Smyth, limma powers differential expression analyses for RNA-sequencing and microarray studies. *Nucleic Acids Res.* **43**, e47 (2015).
- D. Wu, E. Lim, F. Vaillant, M. L. Asselin-Labat, J. E. Visvader, G. K. Smyth, ROAST: Rotation gene set tests for complex microarray experiments. *Bioinformatics* **26**, 2176–2182 (2010).
- L. Alibardi, Review: Limb regeneration in humans: Dream or reality? *Ann. Anat.* **217**, 1–6 (2018).
- K. Muneoka, W. F. Fox, S. V. Bryant, Cellular contribution from dermis and cartilage to the regenerating limb blastema in axolotls. *Dev. Biol.* **116**, 256–260 (1986).
- R. M. White, L. I. Zon, Melanocytes in development, regeneration, and cancer. *Cell Stem Cell* **3**, 242–252 (2008).

48. N. Maki, R. Suetsugu-Maki, H. Tarui, K. Agata, K. del Rio-Tsonis, P. A. Tsonis, Expression of stem cell pluripotency factors during regeneration in newts. *Dev. Dyn.* **238**, 1613–1616 (2009).
49. S. Atanasoski, L. Notterpek, H. Y. Lee, F. Castagner, P. Young, M. U. Ehrengreuber, D. Meijer, L. Sommer, E. Stavnezer, C. Colmenares, U. Suter, The protooncogene *Ski* controls Schwann cell proliferation and myelination. *Neuron* **43**, 499–511 (2004).
50. M. S. Fleming, J. J. Li, D. Ramos, T. Li, D. A. Talmage, S. I. Abe, S. Arber, W. Luo, A RET-ER81-NRG1 signaling pathway drives the development of pacinian corpuscles. *J. Neurosci.* **36**, 10337–10355 (2016).
51. A. Balakrishnan, L. Belfiore, L. Vasan, Y. Touahri, M. Stykel, T. Fleming, R. Midha, J. Biernaskie, C. Schuurmans, ETV5 is not required for Schwann cell development but is required to regulate the Schwann cell response to peripheral nerve injury. *bioRxiv* 2020.09.23.309815 [Preprint]. 24 September 2020; <https://doi.org/10.1101/2020.09.23.309815>.
52. C. E. McGregor, A. W. English, The role of BDNF in peripheral nerve regeneration: Activity-dependent treatments and Val66Met. *Front. Cell. Neurosci.* **12**, 522 (2019).
53. X. Y. Song, F. Li, F. H. Zhang, J. H. Zhong, X. F. Zhou, Peripherally-derived BDNF promotes regeneration of ascending sensory neurons after spinal cord injury. *PLOS ONE* **3**, e1707 (2008).
54. N. L. Sato, S. Inoue, Effects of growth hormone and nutrient on limb regeneration in hypophysectomized adult newts. *J. Morphol.* **140**, 477–485 (1973).
55. R. J. Love, K. S. Jones, Transient inhibition of connective tissue infiltration and collagen deposition into porous poly(lactic-co-glycolic acid) discs. *J. Biomed. Mater. Res. A* **101**, 3599–3606 (2013).
56. Y. Zhang, I. Strehin, K. Bedelbaeva, D. Gourevitch, L. Clark, J. Leferovich, P. B. Messersmith, E. Heber-Katz, Drug-induced regeneration in adult mice. *Sci. Transl. Med.* **7**, 290ra92 (2015).
57. X. Yang, S. Yang, C. Wang, S. Kuang, The hypoxia-inducible factors HIF1 α and HIF2 α are dispensable for embryonic muscle development but essential for postnatal muscle regeneration. *J. Biol. Chem.* **292**, 5981–5991 (2017).
58. A. Ariel, C. N. Serhan, Resolvins and protectins in the termination program of acute inflammation. *Trends Immunol.* **28**, 176–183 (2007).
59. J. R. Monaghan, M. Maden, Visualization of retinoic acid signaling in transgenic axolotls during limb development and regeneration. *Dev. Biol.* **368**, 63–75 (2012).
60. C. Ffrench-Constant, L. Van de Water, H. F. Dvorak, R. O. Hynes, Reappearance of an embryonic pattern of fibronectin splicing during wound healing in the adult rat. *J. Cell Biol.* **109**, 903–914 (1989).
61. A. Altizer, L. J. Moriarty, S. M. Bell, C. M. Schreiner, W. J. Scott, R. B. Borgens, Endogenous electric current is associated with normal development of the vertebrate limb. *Dev. Dyn.* **221**, 391–401 (2001).
62. N. S. Petrosky, R. A. Tassava, C. L. Olsen, Cellular events in denervated limb stumps of *Ambystoma* larvae during re-innervation and subsequent regeneration. *Experientia* **36**, 601–603 (1980).
63. S. E. Iismaa, X. Kaidonis, A. M. Nicks, N. Bogush, K. Kikuchi, N. Naqvi, R. P. Harvey, A. Husain, R. M. Graham, Comparative regenerative mechanisms across different mammalian tissues. *NPJ Regen. Med.* **3**, 6 (2018).
64. Y. Xie, N. Su, J. Yang, Q. Tan, S. Huang, M. Jin, Z. Ni, B. Zhang, D. Zhang, F. Luo, H. Chen, X. Sun, J. Q. Feng, H. Qi, L. Chen, FGF/FGFR signaling in health and disease. *Signal Transduct. Target. Ther.* **5**, 181 (2020).
65. T. Endo, K. Tamura, H. Ide, Analysis of gene expressions during *Xenopus* forelimb regeneration. *Dev. Biol.* **220**, 296–306 (2000).
66. R. Zhang, X. Li, Y. Liu, X. Gao, T. Zhu, L. Lu, Acceleration of bone regeneration in critical-size defect using BMP-9-loaded nHA/Coll/MWCNTs scaffolds seeded with bone marrow mesenchymal stem cells. *Biomed. Res. Int.* **2019**, 7343957 (2019).
67. W. A. Vieira, K. M. Wells, M. J. Raymond, L. de Souza, E. Garcia, C. D. McCusker, FGF, BMP, and RA signaling are sufficient for the induction of complete limb regeneration from non-regenerating wounds on *Ambystoma mexicanum* limbs. *Dev. Biol.* **451**, 146–157 (2019).
68. P. Zhou, J. Wu, Y. Xia, Y. Yuan, H. Zhang, S. Xu, K. Lin, Loading BMP-2 on nanostructured hydroxyapatite microspheres for rapid bone regeneration. *Int. J. Nanomedicine* **13**, 4083–4092 (2018).
69. A. Satoh, A. Makanae, Y. Nishimoto, K. Mitogawa, FGF and BMP derived from dorsal root ganglia regulate blastema induction in limb regeneration in *Ambystoma mexicanum*. *Dev. Biol.* **417**, 114–125 (2016).
70. J. W. Choi, W. S. Jeong, S. J. Yang, E. J. Park, T. S. Oh, K. S. Koh, Appropriate and effective dosage of BMP-2 for the ideal regeneration of calvarial bone defects in beagles. *Plast. Reconstr. Surg.* **138**, 64e–72e (2016).
71. L. Yu, M. Han, M. Yan, E. C. Lee, J. Lee, K. Muneoka, BMP signaling induces digit regeneration in neonatal mice. *Development* **137**, 551–559 (2010).
72. L. Yu, L. A. Dawson, M. Yan, K. Zimmer, Y. L. Lin, C. P. Dolan, M. Han, K. Muneoka, BMP9 stimulates joint regeneration at digit amputation wounds in mice. *Nat. Commun.* **10**, 424 (2019).
73. J. A. Lehoczyk, C. J. Tabin, Lgr6 marks nail stem cells and is required for digit tip regeneration. *Proc. Natl. Acad. Sci. U.S.A.* **112**, 13249–13254 (2015).
74. C. P. Dolan, L. A. Dawson, K. Muneoka, Digit tip regeneration: Merging regeneration biology with regenerative medicine. *Stem Cells Transl. Med.* **7**, 262–270 (2018).
75. A. S. Tseng, W. S. Beane, J. M. Lemire, A. Masi, M. Levin, Induction of vertebrate regeneration by a transient sodium current. *J. Neurosci.* **30**, 13192–13200 (2010).
76. A. Tseng, M. Levin, Cracking the bioelectric code: Probing endogenous ionic controls of pattern formation. *Commun. Integr. Biol.* **6**, e22595 (2013).
77. M. Han, X. Yang, G. Taylor, C. A. Burdsal, R. A. Anderson, K. Muneoka, Limb regeneration in higher vertebrates: Developing a roadmap. *Anat. Rec. B New Anat.* **287B**, 14–24 (2005).
78. M. A. Storer, N. Mahmud, K. Karamboulas, M. J. Borrett, S. A. Yuzwa, A. Gont, A. Androschuk, M. V. Sefton, D. R. Kaplan, F. D. Miller, Acquisition of a unique mesenchymal precursor-like blastema state underlies successful adult mammalian digit tip regeneration. *Dev. Cell* **52**, 509–524.e9 (2020).
79. K. Muneoka, C. H. Allan, X. Yang, J. Lee, M. Han, Mammalian regeneration and regenerative medicine. *Birth Defects Res. C Embryo Today* **84**, 265–280 (2008).

Acknowledgments: We would like to thank E. Switzer for animal husbandry and maintenance, R. Colon and J. Mandal for general laboratory assistance, N. Li from Tufts University Histology Core for histological processing support, and members of the Levin and Kaplan laboratories for helpful comments. We would also like to express our gratitude to I. Pinz and T. Henderson from Maine Medical Center Research Institute for micro-CT measurements. We would also like to thank C. Serhan for his insights and expertise. This research was supported by the Allen Discovery Center program through The Paul G. Allen Frontiers Group (12171). **Funding:** We gratefully acknowledge the support from the NIH (R01 AR005593, R01 AR061988, and P41EB027062) and the W.M. Keck Foundation (5903). **Author contributions:** N.J.M., D.L.K., and M.L. conceived the ideas and specific experimental approaches. N.J.M., H.J.V., K.A.M., A.G., A.W.K., and Q.L.P. carried out the experiments and data collection. M.M.S., C.R.-I., and N.J.M. performed data analysis. N.J.M., D.L.K., and M.L. wrote the manuscript. **Competing interests:** M.L., D.L.K., and N.J.M. are inventors on a pending patent related to this work filed by Tufts University (PCT/US2020/063665). D.L.K. and M.L. are cofounders of the company MorphoCeuticals Inc., which operates in the regenerative medicine space and does research relevant to the subject of this paper. The authors declare no other competing interests. **Data and materials availability:** All data needed to evaluate the conclusions in the paper are present in the paper and/or the Supplementary Materials.

Submitted 27 April 2021
 Accepted 6 December 2021
 Published 26 January 2022
 10.1126/sciadv.abj2164